Reynolds-Averaged Navier Stokes Simulation of Scramjet Inlet Flowfield

Krishnendu Sinha * and Vadivelan C †

Abstract

The forebody of a hypersonic vehicle based on scramjet propulsion acts as an external compression inlet for the engine. A typical configuration consists of compression ramps and wedges. The flow field generated by these compression surfaces is quite complex. In the absence of experimental data, computational fluid dynamics serves as a valuable tool in understanding the flow physics and predicting the characteristics of the inlet configuration. In this paper, a generic hypersonic forebody geometry consisting of compression ramps and side fences is investigated. The shock and surface flow pattern is examined in detail, followed by the surface pressure and heat transfer prediction on the geometry.

1 Introduction

In a hypersonic vehicle based on Supersonic Combustion Ramjet (scramjet) propulsion system, the forebody acts as an external inlet for the engine. The forebody is designed to achieve maximum mass capture by the engine and efficient compression of the incoming flow. The bow shock from the nose compresses the gas on the underside of the vehicle forebody. This is followed by further compression in the internal inlet of the engine. Additional surfaces, such as side fences, are used to achieve three-dimensional compression as well avoid the air spillage from the side of the vehicle. For optimum performance of the inlet, the shock waves generated by different parts of the forebody should intersect at the cowl lip.

The flow around the vehicle forebody is complex due to the presence of multiple shock waves generated by the nose, ramp sections and fences. Intersection of these shock waves among themselves can often result in a complex three-dimensional flow pattern. The flight Reynolds number is often high enough for the boundary layer on the vehicle to be turbulent. The adverse pressure gradient of the shock waves can result in local separation of the turbulent boundary layer. This degrades the pressure recovery of the inlet and can lead to local high heating rate to the vehicle walls.

*Assistant Professor, Indian Institute of Technology Bombay, krish@aero.iitb.ac.in
†Research Assistant, Indian Institute of Technology Bombay, velan@aero.iitb.ac.in

Experimental study of scramjet configurations at realistic flight conditions is often prohibitively expensive, if not unattainable in ground-based facilities. Computational fluid dynamics is therefore extensively used to study scramjet flowfields and to predict performance parameters. There are however several challenges in terms of numerical, physical and geometric modeling. Robust and accurate CFD methods are needed to capture the shock waves and their interactions. Prediction of turbulent heating and skin friction in three-dimensional boundary layers is challenging for turbulence models. This is especially true in high speed flows because of compressibilty effects in shock waves and possible shock induced flow separation. Geometric complexity of scramjet inlets requires sophisticated griding techniques and large scale parallel simulation capability to achieve high quality results.

In this paper, we study the inlet flow field of a generic scramjet based hypersonic vehicle with compression ramps and side fences. The goal is to generate high-quality solution of a complex practical geometry, and use it to study the underlying flow physics. The geometric configuration is presented next, followed by a description of the solution methodology and generation of computational grid. In-house Reynolds-averaged Navier Stokes (RANS) code with multi-block structured grid is used to simulate the three-dimensional flow field. Results are presented in terms of the shock wave pattern and surface flow streamlines. The turbulent boundary on the vehicle surface and the resulting heat transfer and skin friction coefficients are computed, and the solution is analyzed for possible local flow separation. Of specific interest is the high-pressure region at the ramp-fence corner.

2 Geometric Configuration

The scramjet inlet considered in this work is shown in Fig. 1(a). It consists of two compression ramps of 11.86 and 13.75 degrees respectively. Two side fences are attached on the second ramp which lead to the cowl and internal compression inlet of the engine. The current simulations consider only the ramps and fences which constitute the external part of the scramjet inlet. The top and side surfaces are relatively flat. The main focus of this work is the lower forebody surface and the relevant geometric parameters are identified in Fig. 1(a). Due to symmetry in the geometry and incoming freestream flow, only one half of the configuration is simulated. The free stream conditions correspond to a Mach number of 6.5, angle of attack 5 degrees, density of 0.0122 kg/m^3, and temperature of 237 K. The wall temperature is assumed to be constant at 300 K.

3 Simulation Methodology

In-house finite volume code is used to solve Favre-averaged Navier-Stokes equations for the mean flow, and the Spalart-Allmaras model for turbulence closure. Details of the turbulence model are given in [1] and are omitted here for the sake of brevity. Inviscid fluxes are computed using a modified (low-dissipation) form of the Steger-Warming flux splitting approach, and the turbulence model equations are fully coupled to the mean flow equations. The method is second order accurate both in stream-wise and wall normal directions. The viscous fluxes and the turbulent source terms are evaluated using second order accurate central differencing and the implicit Full Matrix Data Parallel method is used to obtain steady-state solution. The details of the formulation are given in Ref. [2]. The code has multi-block capability and is implemented in parallel using Message Passing Interface. It has been successfully applied to several supersonic and hypersonic flow computation and a recent validation in a axi-symmetric cone-flare geometry is presented in [3] .

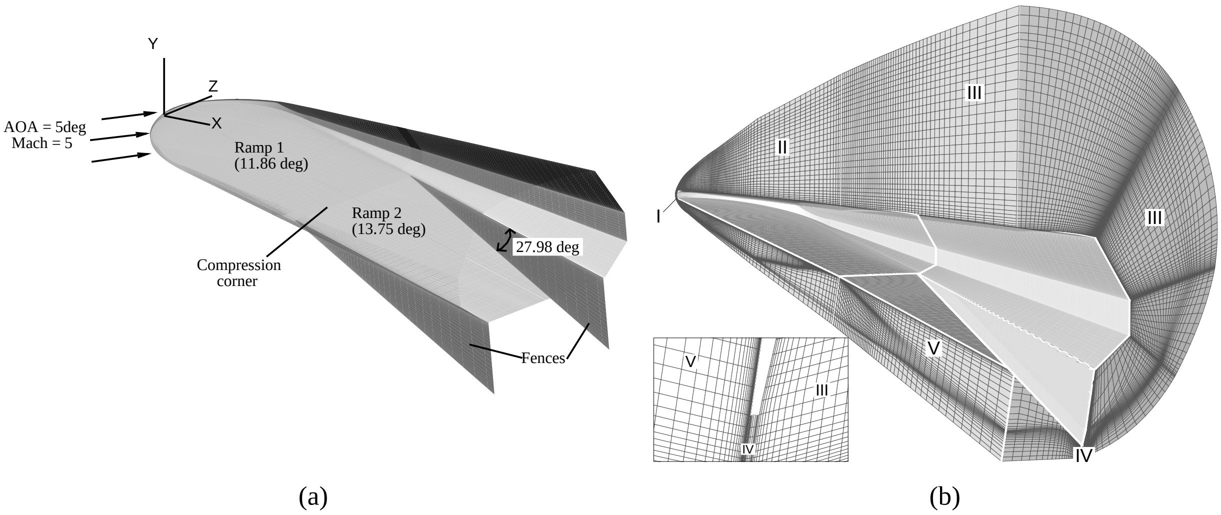

Figure 1: Scramjet inlet: (a) geometry consisting of two compression ramps and two fences and (b) the multi-block grid topology used in the simulatoin. Inset shows magnified view of the fence tip region.

3.1 Grid generation

The volume grid around the three-dimensional scramjet inlet configuration is generated using Gridgen software. It consists of five blocks with point-matching at inter-block boundaries, and are designed based on the geometric and flow features of the inlet (see Fig. 1(b)). A C-type grid block II is used on the first ramp with a separate grid block I at the nose to avoid grid singularity in the stagnation region. Block III spans the region downstream of the ramp corner, on the top surface and side of the vehicle. Two additional grid blocks are used in the vicinity of the fence. Grid block V is placed between the fence and the vehicle mid-plane to allow careful grid refining in this region of interest, and grid block IV is required to model the finite thickness at the fence tip.

The nose region is critical because of high three-dimensional geometric curvature as well as presence of the strong normal shock. The vicinity of the nose stagnation point is covered by grid block I with 100x20 surface points. Block I has almost uniform mesh in both streamwise and spanwise direction with cell size around 0.02 of nose radius to capture the highly curved bow

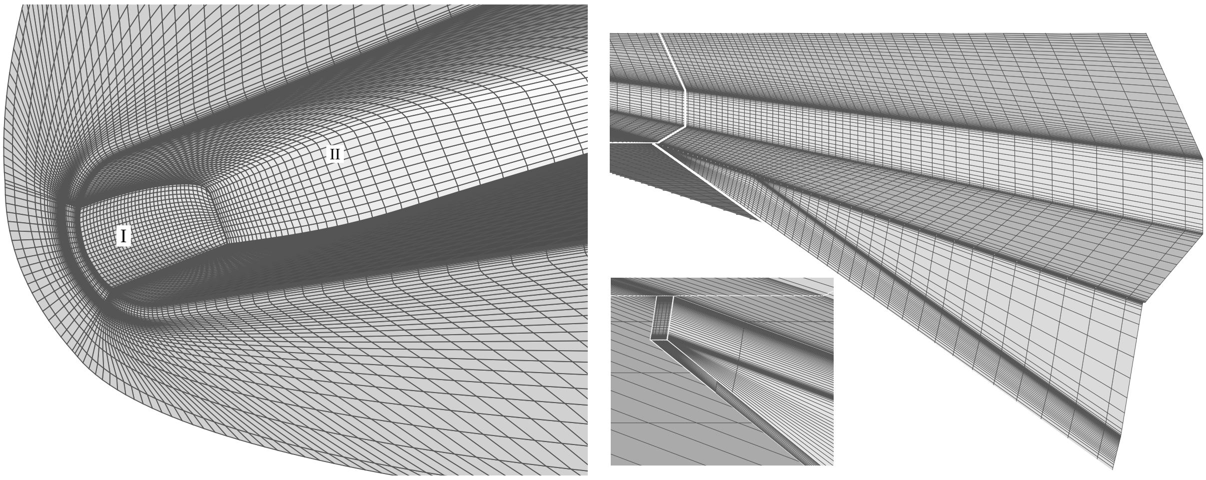

(a) (b)

Figure 2: Magnified view of the grid in the (a) nose and (b) fence region to highlight grid blocks.

shock at the nose. A coarser and larger block I spanning the stagnation region as well as part of the expansion regions resulted in poor resolution of the shock curvature, surface heat transfer distribution and highly skewed cells that led to problems in iterative convergence. On the other hand, very fine surface mesh in the stagnation region often causes numerical problems.

Grid block II consists of 120x220 surface points. In the streamwise direction, the grid points are clustered near the nose expansion regions and the corner between the two ramps. The grid point distribution is based on two-dimensional simulation of the mid-plane section as described below. In the spanwise or circumferential direction (j), fine mesh is used at the sharp edges at the vehicle side and relatively coarse mesh is used near the symmetry plane in the middle. The bottom compression surface is the primary focus of these simulations. There are 50 streamwise (i) points downstream of the ramp corner, and the 220 j-points are split into block III (162 points), block IV (12 points) and block V (46 points). The normal j-spacing adjacent to the fence is maintained at 0.05mm on both outside and inside of the fence. The grid spacing is varied to study its effect on the flow solution.

In the normal direction, the grid point distribution is determined by the requirements of resolving the shock wave and boundary layer, and the geometric constraint of the fence tip. The fence is triangular in shape with its tip located at the corner between the two ramps. A structured mesh on the fence surface will have a grid singularity at the tip. This is avoided by approximating the singularity by a finite but small height of 1mm. This is more than two orders smaller in magnitude than other relevant dimensions of the inlet, and therefore is not expected to alter the overall solution significantly.

The boundary layer adjacent to the vehicle walls is captured most accurately by a very fine orthogonal mesh. This is generated by extruding volume cells from the surface grid described above with small grid cell height at the surface and a controlled exponential stretching normal to the wall. The mesh requirements in the outside inviscid region are much less stringent except in the vicinity of the shock wave. The normal grid spacing at the shock should be small to capture the high gradient and the grid lines in the tangential directions should be aligned parallel to the shock to minimise numerical error. This can be achieved by placing the outer boundary of the domain close to the shock and carefully aligning it with the shock shape. This process is quite challenging for a shock wave generated around a complex three-dimensional geometry with multiple grid blocks. With considerable effort, the outer boundary has been manually tailored to the shock wave to a large extent.

Ideally, the extrusion layer should encompass the entire boundary layer. This is however not possible in the current configuration because the boundary layer thickness at the end of the second ramp is about 28.3 mm. This is larger than that the shock stand-off distance at the nose, which precludes having a fine mesh in the outer part of the extrusion layer for the shock. As a result, only the near-wall high gradient region of the turbulent boundary layer on the compression ramps are gridded using the orthogonal extrusion layer.

The height of the extrusion layer is further limited by the geometric constraint of a small fence tip. The 1 mm height of the fence tip has to accommodate the extrusion layer and all the grid lines that span the fence surface (see Fig. 2(b)). The fence leading edge is a single grid line. This allows accurate description of the leading edge geometry as well as a better resolution of the high gradients at the inception of fence boundary layer at the leading edge (in this region). The fence surface is spanned by 96 points along this height (k-direction). As expected, the grid point distribution is this direction is very fine at the fence tip and becomes coarse towards the exit plane. The total number of points in the k-direction is 150 with the remaining 54 points distributed between the fence leading edge and the outer boundary.

The multiblock volume grid is generated using the procedures described above. The grid blocks are often sub divided into smaller domains for careful gridding, especially in the vicinity of the fence outer surface and the side expansion corner. Better quality mesh is generated in these sub-domains and they are then combined to form the five block topology. The full three-dimensional multiblock grid consists of about 4 million grid points.

4 Simulation Results

Figure 3 shows the bow shock and the shock generated by the ramp corner in terms of the Mach number contours on the mid-plane. The bow shock angle on the lower surface is 24 deg and the oblique shock at the ramp corner is close to the angle of the fence leading edge. This oblique shock merges with the bow shock at x = 1.37 m resulting in a Edney Type VI interaction to steepen the outer shock and a weak expansion wave is generated. A magnified view of the Mach number contours in the vicinity of the nose is also shown in Fig. 3. Careful alignment of the grid lines to the shock shape captures the bow shock accurately and eliminates spurious error in the nose stagnation region. An entropy layer is generated by the bow shock curvature at the nose and it merges with the turbulent boundary layer that develops on the ramp surfaces.

The structure of the bow shock in several cross-sectional planes along the length of the second ramp is shown in Fig. 4. The bow shock shape changes from highly elliptic near the tip of the vehicle (not shown here) to circular towards the end of the fore body. This corresponds to the varying aspect ratio of the vehicle. At x=0.48, which corresponds to the ramp corner,

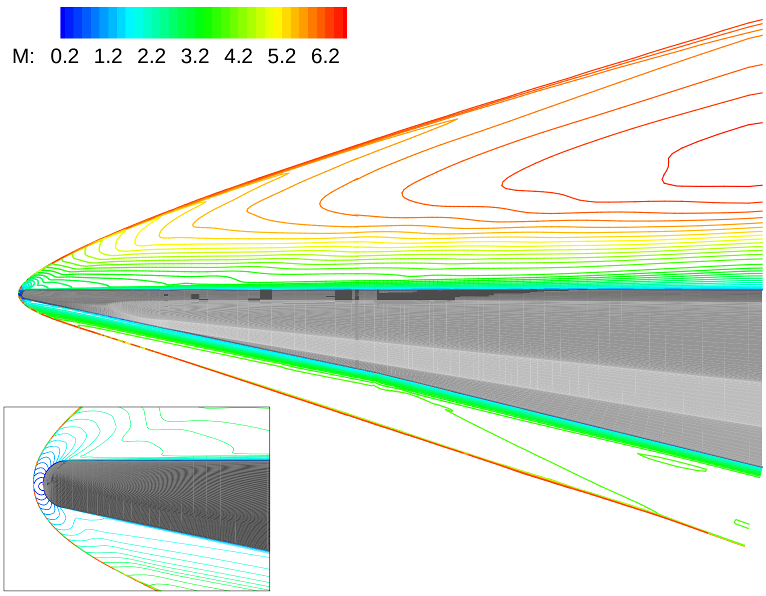

Figure 3: Mach number distribution on the vehicle mid-plane with inset showing a magnified view of the nose region.

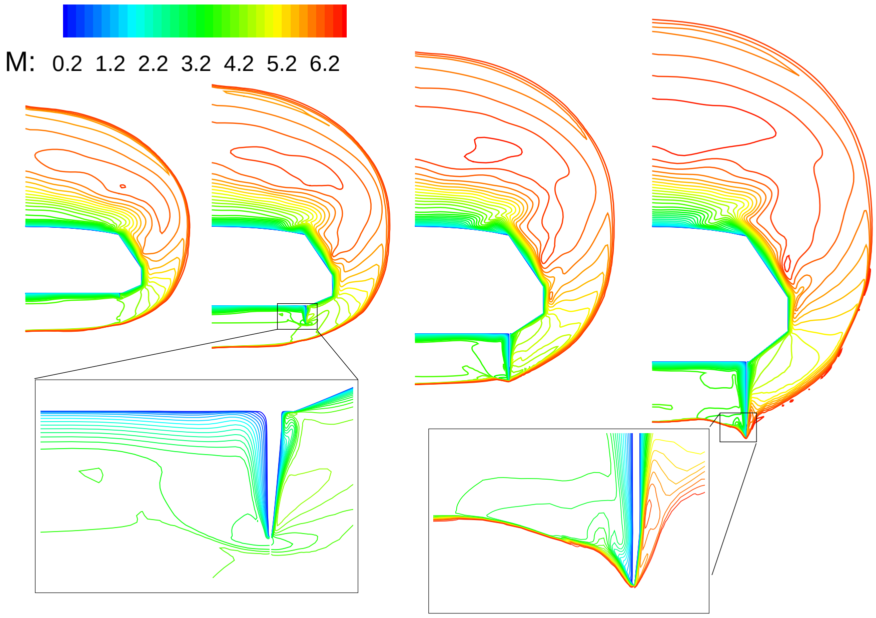

Figure 4: Mach number contours on different cross-sectional planes (normalized x values of 0.48, 0.69, 0.88 and 1.0) along the second compression ramp. Insets show magnified regions at the fence.

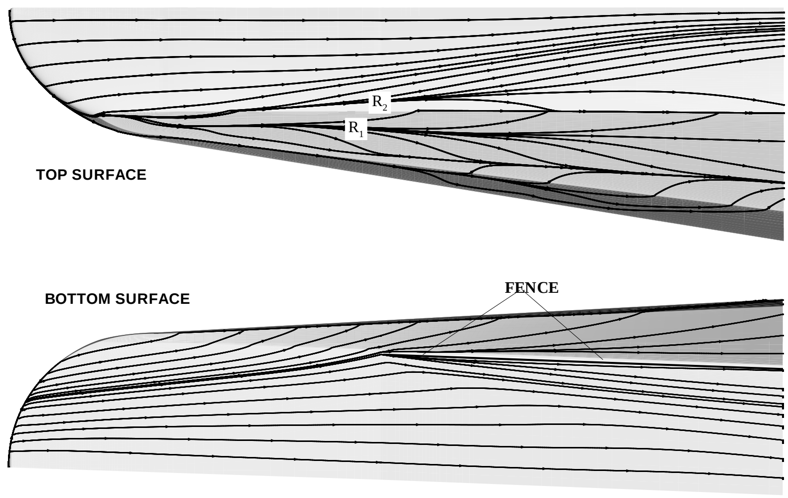

Figure 5: Surface streamlines on the vehicle body showing both the top and bottom surfaces.

the high compression region generated by the strong shock extends over majority of the ramp surface. The shock weakens as the flow expands around the vehicle sides. The weak shock generated by the ramp corner is visible in the x=0.69 section. It is relatively flat and two-dimensional over the ramp, but is curved outward near the fence tip. This is becuase of the high compression region formed near the fence that pushes the flow and shock outward. The curved shock merges with the outer bow shock in the x=0.88 section. Further downstream, the fence tip extends outside of the vehicle bow shock, and is exposed to the freestream. A magnified view of the fence tip at the exit location shows the oblique shocks generated by the fence tip and how it merges with and distorts the bow shock from the vehicle nose. The fence thus effectively isolates the highly compressed flow on the ramp surface from the expansion around the vehicle sides.

The entropy and boundary layers on the vehicle wall is also seen in the cross section. Entropy layer is thin and strong (almost uniform thickness) on the lower surface. It merges with the boundary layer on the fence to thicken at the fence-ramp corner (see inset A in Fig. 4). On the top surface, effect of flow expansion results in a larger region of temperature and Mach number variation. Distortion (thickening/thinning) of the boundary layer can also be seen on the sharp edges on the vehicle sides. These are due to local flow separation and reattachment, for example, at the corner of the top surface. The surface stream lines in Fig. 5 show this effect more clearly. Converging streamlines correspond to local flow separation and diverging streamlines represent cross-flow re-attachment.

On the lower surface the flow is mostly axial near the midplane, but there is substantial spillage on the vehicle side on the first ramp. The presence of the fence inhibits flow spillage from the second ramp and results in additional compression of the gas. The span-wise pressure gradient caused by the fence is however small enough for the boundary layer to remain attached on the second ramp. The flow pattern on the inner compression surface of the fence as well as

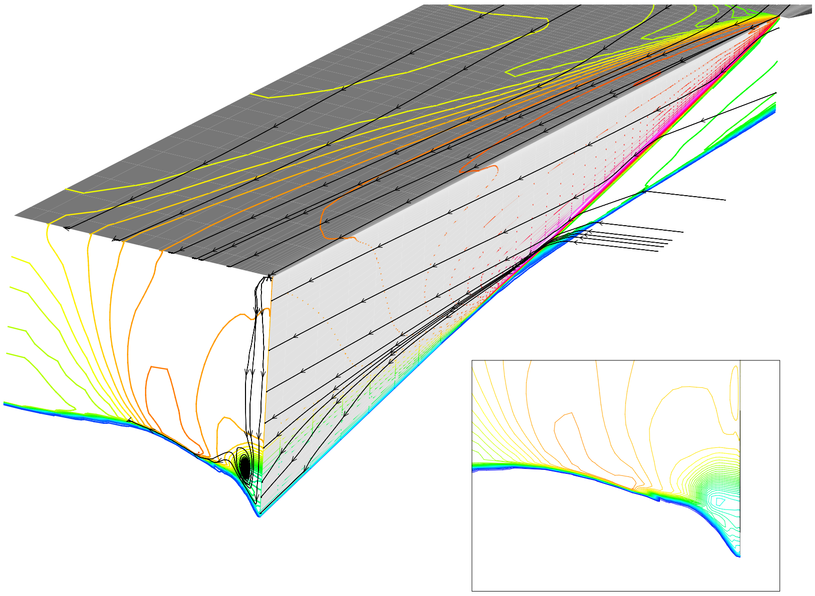

Figure 6: Pressure contours and representative streamlines are plotted on the second ramp, fence inner surface and the exit plane to show the shock/expansion waves.

the exit plane is presented in Fig. 6 in terms of the pressure contours and surface streamlines. The 5 degree angle of attack free-stream flow is deflected by the bow shock and then by the corner shock, which is marginally downstream of the fence leading edge. The corner shock results in high pressure slightly downstream of the fence leading edge. The bow shock becomes stronger on intersecting with the corner shock and it then interacts with the oblique shock from the fence leading edge. The pressure contours in the exit plane show this shock-shock interaction and the resulting expansion waves that are transmitted to the fence surface. Foot print of the expansion waves can be seen on the fence wall downstream of the bow shock impingement location. The resulting favorable pressure gradient deflects the highly compressed flow at the fence-ramp corner towards the fence leading edge. The flow is then deflected back by the shock waves to form a vortical structure, as can be seen in the streamlines plotted in the exit plane.

Figure 7(a) shows the pressure on the bottom surface along the mid-plane section as a function of the x-coordinate, with x=0 denoting the tip of the vehicle. The pressure along the first compression ramp is mostly uniform. Pressure increases at the ramp corner followed by a gradual decrease along the second ramp. There is a small increase in mid-plane pressure towards the end of the second ramp due to side compression by the fence. This is absent in the simulation of the fore body geometry without fences. Both simulations of the three-dimensional geometry yield pressure that is about 5-7% lower than two-dimensional inviscid theory, denoted by solid triangle in the figure. Two-dimensional simulations of the mid-plane geometry as well as of the compression ramps match the inviscid theory well. This is because of weaker bow shock in the three-dimensional finite-span geometry than the two-dimensional configurations.

The spanwise variation of pressure on the first ramp downstream of the bi-curvature nose

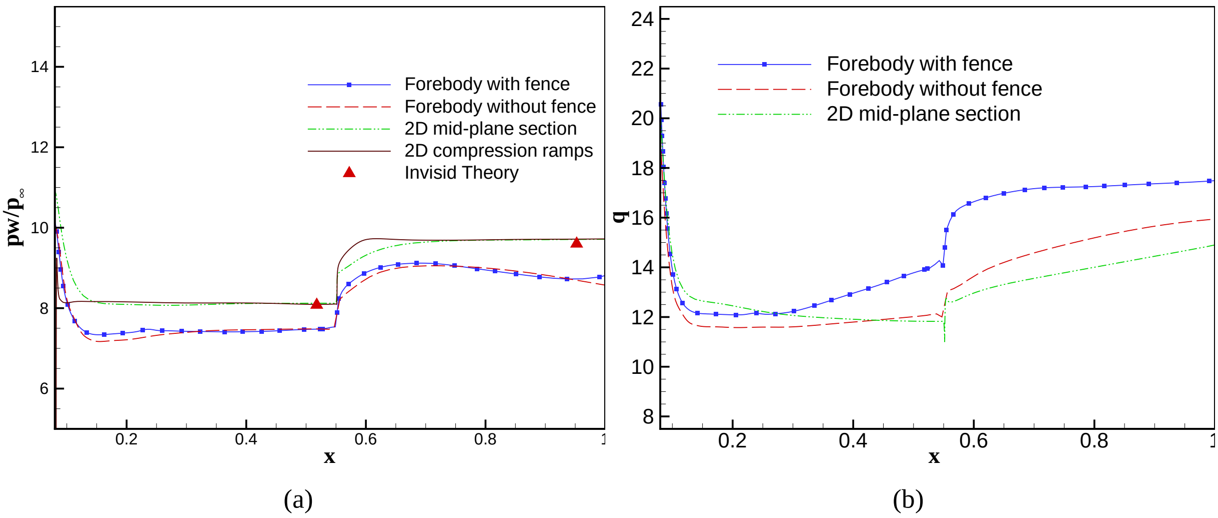

Figure 7: Normalized pressure and heat transfer along the mid-plane bottom section. Data from other simulations like forebody without fences, two-dimensional computation of the mid-plane section, and two-dimensional compression ramps are presented for comparison.

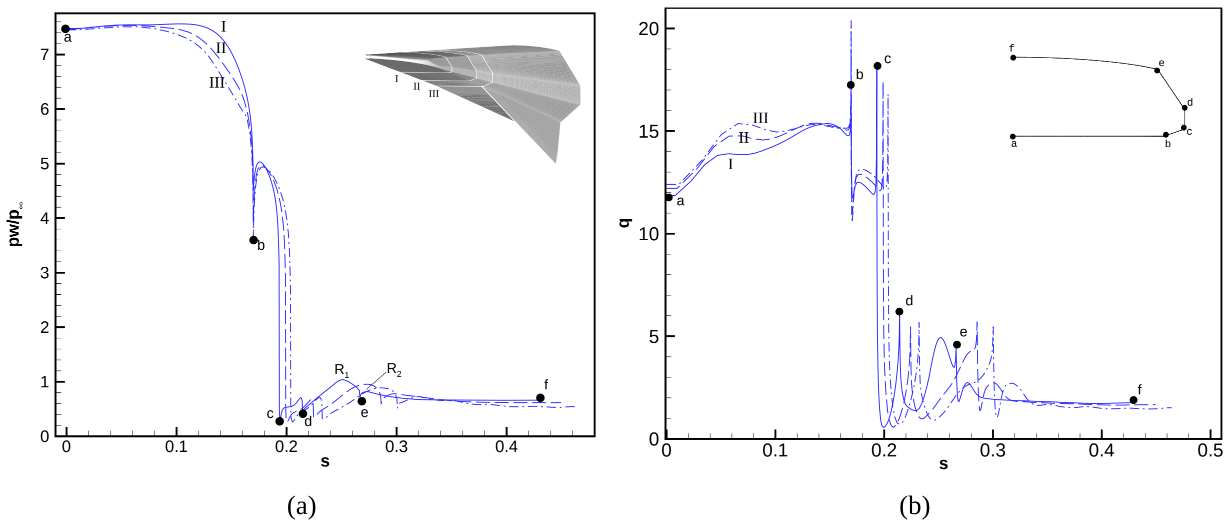

Figure 8: Normalised surface pressure and heat trasnfer distribution around the vehicle at different axial locations (shown by white lines in the inset) on the first ramp. The geometric features on the vehicle surface are also identified in terms of the points a through f.

region is presented in Figure 8(a). Normalized pressure is plotted as a function of the arc length measured from the bottom mid-plane section (s=0). Data is presented along three x=constant sections identified in the inset vehicle geometry. A large spanwise portion of the ramp surface is close to the mid-plane pressure, but the effect of flow spillage and the associated reduction in pressure near the vehicle side is clear. The extent of this cross-flow expansion region increases to about 50% at section III immediately upstream of the ramp corner. In section I pressure distribution, a sharp drop at point b corresponds to the expansion at the edge of ramp. Similar pressure minima are observed at the subsequent expansion corners c, d, and e around the vehicle. On the other hand, local maxima in surface pressure correspond to flow reattachment, for example, at points R_1 and R_2 in Fig. 5. The pressure on the top leeward surface is fairly uniform and below the free stream value. All the three sections show the same pressure pattern. The s coordinate is stretched for downstream sections II and III because of increase in the vehicle cross-section.

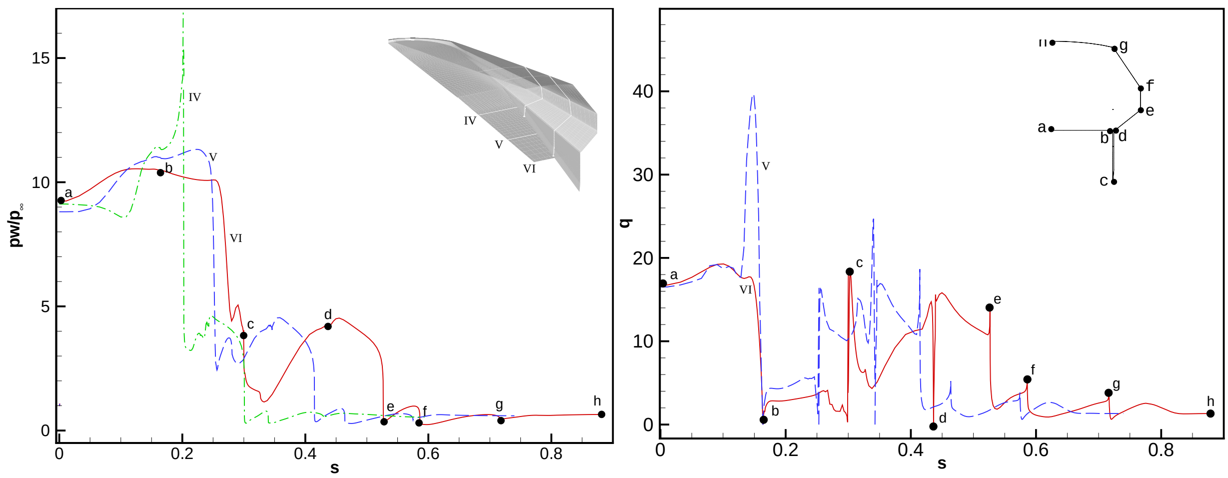

(a)

(b)

Figure 9: Normalised surface pressure and heat transfer distribution around the vehicle at different axial locations (shown by white lines in the inset) on the second ramp. The geometric features on the vehicle surface are also identified in terms of the points a through h.

Spanwise pressure variation downstream of the ramp corner is presented in Fig. 9(a). The three axial stations shown in the inset forebody geometry correspond to 1/3, 2/3 and the end of the second ramp. Note that the fence inner bc and outer cd surfaces are also included in the plots. The mid-plane pressure values are higher than those on the first ramp, and there is an increase in pressure from the mid-plane to the ramp-fence corner due to the additional compression by the fence. This trend is in contrast to that observed on the first ramp, where cross-flow expansion causes the pressure to decrease away from the mid-plane section. The fence pressure rise is quite high at section IV probably due to the corner shock located close to the fence leading edge, followed by a rapid expansion at the fence tip. At section VI, a similar pressure drop is observed slightly inside of the fence tip c. This is because of the expansion waves from the interaction of fence tip shock and the bow shock. The magnitude of pressure at the ramp-fence corner decreases and the extent of side-compression region grows with increasing x. At the exit locaton VI, the effect of the fence compression is felt across the entire span of second ramp. The geometric locations a through h are identified on the pressure curve for section VI. The pressure pattern at the expansion corners e, f and g are similar to that observed at the corresponding locations in Fig. 8(a). A broad pressure peak centered at around the corner d between fence outer surface and side surface is caused by flow separation on the fence surface and corresponding reattachment on the de segment of the vehicle wall. This pressure peak is prominently visible at all the three sections.

The heat transfer results plotted in Fig. 8(b) show values in the range of 12-15 $\mathrm{W/cm^2}$ along the first ramp. There is sharp peak in heating rate at the expansion corner b. Similar heat transfer peaks are also seen at subsequent corners c through e, as identified for section I. The heating rate distribution at sections II and III show a similar trend. The heat level progressively decreases through the expansion corners to reach about 2 $\mathrm{W/cm^2}$ on the top surface. There are additional heat transfer maxima at cross-flow reattachment points, for example, R_1 and R_2. The heat transfer rate on the second compression ramp (see Fig. 9(b)) is in the range 18-20 $\mathrm{W/cm^2}$ except for the peak value of 40 $\mathrm{W/cm^2}$ at $s = 0.25$ at cross-section V. This may be because of the compression near the fence. There is a decrease in heat transfer rate near points b and d, which are located at the ramp-fence corner. The heating pattern observed otherwise follow the flow expansion and separation/reattachment pattern discussed earlier.

5 Conclusions

Three-dimensional simulations are performed using in-house Reynolds-averaged Navier-Stokes code to study the flow on a scramjet vehicle forebody. The main focus is on the compression ramps and side fences. Multi-block grid with about 4 million points is generated with careful grid alignment and refinement in high gradient regions. Multiple shock waves are generated by the forebody nose, compression corners, and fences. Interaction of these shock waves lead to a complex pattern of shocks and expansion waves. The resulting flow on the vehicle surface show multiple regions of cross-flow separation and reattachment,especially on the side walls. Variation of surface pressure and heat transfer correlate well with the underlying flow pattern.

References

[1] Spalart and Allmaras. A one-equation turbulence model for aerodynamic flows. *AIAA Paper*, 92-0439, 1992.

[2] Sinha K. and Candler G.V. Convergence improvement of two-equation turbulence model calculations. *AIAA Paper*, 98-2649, 1998.

[3] Sinha K. ”Shock unsteadiness model applied to hypersonic shock-wave/turbulent boundary layer interactions”. *AIAA Paper*, 2006-0126, 2006.